1-4-2021

n-Type Charge Transport in Heavily *p*-Doped Polymers

Zhiming Liang
University of Kentucky, leungchiminh@gmail.com

Hyun Ho Choi
Rutgers University

Xuyi Luo
Purdue University

Tuo Liu
University of Kentucky, tli252@uky.edu

Ashkan Abtahi
University of Kentucky, a.abtahi@uky.edu

See next page for additional authors

n-Type Charge Transport in Heavily *p*-Doped Polymers

Digital Object Identifier (DOI)
https://doi.org/10.1038/s41563-020-00859-3

Notes/Citation Information
Published in *Nature Materials*, v. 2021.

Authors
Zhiming Liang, Hyun Ho Choi, Xuyi Luo, Tuo Liu, Ashkan Abtahi, Uma Shantini Ramasamy, J. Andrew Hitron, Kyle N. Baustert, Jacob L. Hempel, Alex M. Boehm, Armin Ansary, Douglas R. Strachan, Jianguo Mei, Chad Risko, Vitaly Podzorov, and Kenneth R. Graham

n-Type Charge Transport in Heavily *p*-Doped Polymers

Zhiming Liang,[a] Hyun Ho Choi,[b] Xuyi Luo,[c] Tuo Liu,[a] Ashkan Abtahi,[a,d] Uma Shantini Ramasamy,[a,e] J. Andrew Hitron,[f] Kyle N. Baustert,[a] Jacob L. Hempel,[d] Alex M. Boehm,[a] Armin Ansary,[d] Douglas R. Strachan,[d] Jianguo Mei,[c] Chad Risko,[a,e] Vitaly Podzorov,[b] and Kenneth R. Graham*[a]

Author affiliations

*Corresponding author

[a]Department of Chemistry, University of Kentucky, Lexington, Kentucky 40506, USA
E-mail: Kenneth.Graham@uky.edu

[b]Department of Physics and Astronomy, Rutgers University, Piscataway, New Jersey 08854, USA.

[c]Department of Chemistry, Purdue University, West Lafayette, Indiana 47907, USA

[d]Department of Physics & Astronomy, University of Kentucky, Lexington, Kentucky 40506, USA

[e]Center for Applied Energy Research, University of Kentucky, Lexington, Kentucky 40511, USA

[f]MH Catalyst, LLC, Lexington, Kentucky 40511, USA

Abstract:

It is commonly assumed that charge-carrier transport in doped π-conjugated polymers is dominated by one type of charge carrier, either holes or electrons, as determined by the chemistry of the dopant. Here, through Seebeck coefficient and Hall effect measurements, we show that mobile electrons significantly contribute to charge-carrier transport in π-conjugated polymers that are heavily *p*-doped with strong electron acceptors. Specifically, the Seebeck coefficient of several *p*-doped polymers changes sign from positive to negative as the concentration of the electron accepting $FeCl_3$ or $NOBF_4$ dopant increases, while Hall effect measurements for the same *p*-doped polymers reveal that electrons become the dominant delocalized charge carriers. Ultraviolet and inverse photoelectron spectroscopy measurements show that doping with electron acceptors results in

elimination of the transport gap at high doping concentrations. This approach of heavy *p*-type doping is demonstrated to provide a promising route to high-performance *n*-type organic thermoelectric materials.

Charge-carrier transport in materials based on π-conjugated polymers (CPs) has been of substantial interest since the discovery of electrically conductive CPs one-half century ago,[1-4] with the reported transport mechanisms ranging across metallic,[2, 3, 5-8] semi-metallic,[9] and hopping-type regimes.[3, 10-13] Here, metallic and semi-metallic suggest a band-like transport mechanism with the Fermi energy (E_F) lying within one band of electronic states for a metal, or at the intersection of two bands of electronic states for a semi-metal.[9] CPs that possess metallic or semi-metallic properties are generally composed of mesoscopic crystalline domains with metallic transport separated by disordered amorphous regions that operate in the hopping-type transport regime and limit macroscopic transport.[3, 14, 15] By contrast, charge carriers in fully amorphous and many semi-crystalline CPs are kinetically limited by hopping transport across all scales.

In addition to the transport mechanism, it is not always clear what polarity of charge carriers dominate conduction in CPs.[4] Most often the charge-carrier polarity is simply inferred from whether the dopant is an oxidizing (*p*-type doping) or reducing (*n*-type doping) agent, though this is not always a correct assumption. Here, we unequivocally demonstrate that heavy *p*-doping of CPs can induce mobile electrons.

The Seebeck coefficient (α), which is influenced by the energy distribution of charge carriers relative to E_F, provides important information on both the charge-carrier transport

mechanisms and energetic disorder in CPs.[3, 16-19] In addition, the thermoelectric (TE) figure of merit, *ZT*, is proportional to α^2. The sign of α is often used as a probe of charge-carrier polarity, as typically α is positive in *p*-type and negative in *n*-type semiconductors. However, two recent reports observed a change in the sign of α from negative to positive as the concentration of a reducing dopant was increased in different CPs.[20, 21] Although the power factors in these reports are relatively low for both *n*-type and *p*-type performance ($\leq$ 0.81 $\mu W\ m^{-1}\ K^{-2}$), they highlight the potential of using *n*-type dopants to develop *p*-type TE materials and *vice versa*. Furthermore, these reports bring about fundamental questions concerning charge-carrier transport in CPs.

Polyaniline (PANI) is a widely studied CP that can show a change in the sign of α without changing the dopant type.[3, 6, 14, 16, 22, 23] Here, the sign of α can change based on pH,[6] the degree of crystallinity,[3] and even the direction of measurement in aligned PANI samples.[17] This transition from positive to negative α is attributed to the relative contributions of metallic and hopping transport.[3, 16, 17] However, no reports where α changes sign present direct experimental measurements of whether electrons or holes dominate conduction; and, as will be explained later, a negative α does not necessarily imply that electrons dominate the electrical conductivity (σ).

Herein, we demonstrate that the sign of α in many CPs can change from positive to negative by increasing the concentrations of either the oxidizing ferric chloride ($FeCl_3$) or nitrosonium tetrafluoroborate ($NOBF_4$) dopants. Notably, heavily doped PDPP-4T (Fig. 1) showcases both a high *p*-type power factor (PF) of 24.5 $\mu W\ m^{-1}\ K^{-2}$ and a high *n*-type PF of 9.2 $\mu W\ m^{-1}\ K^{-2}$ using the same $FeCl_3$ dopant. We explore the origin of this sign change in α

through ultraviolet and inverse photoelectron spectroscopy (UPS and IPES, respectively), Hall effect measurements, density functional theory (DFT) calculations, electron paramagnetic resonance (EPR), and UV-Vis-near-IR absorbance (UV-Vis-NIR). The UPS and IPES measurements show that the distributions of occupied and unoccupied states converge as the doping concentration in the sample increases, leading to a vanishing transport gap at high doping levels. With minimal transport gap, holes and electrons can populate the occupied and unoccupied manifolds of states, respectively, and both carrier types can contribute significantly to σ. Based on the Hall effect, EPR, and α measurements, we propose a model whereby delocalized electrons form in the crystalline regions at moderate and high doping levels and compete with hopping-type transport of holes in the amorphous regions to ultimately determine whether α is negative or positive.

The CPs displayed in Fig. 1 were selected owing to their diverse chemistry, differing morphologies, differing charge-carrier mobilities, and wide variations in electron affinities (EA), ionization energies (IE), and transport gaps. Data derived from UPS, IPES, and UV-Vis-NIR spectra of the pristine CPs are provided in Supplementary Table S1 and the spectra are displayed in Fig. S2 and S3. $FeCl_3$ was used as the primary dopant for its ability to dope polymers to high doping concentrations,[24] although $NOBF_4$-doped CPs exhibit similar trends. The polymers were doped with $FeCl_3$ at doping ratios up to 1.5, where the doping ratio refers to the molar ratio of dopant molecules to aromatic rings from the polymer.

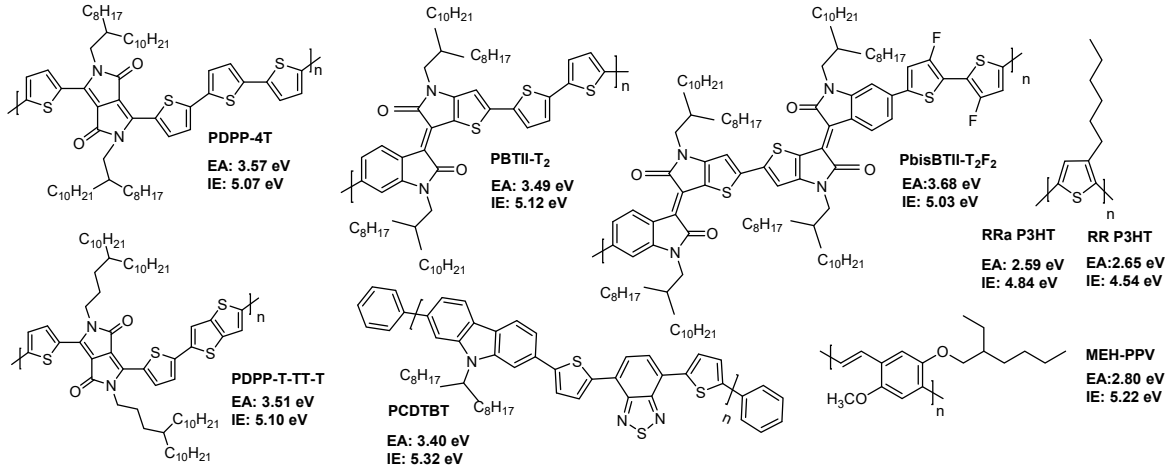

Fig. 1: Polymers and their EA and IE values, as measured for the undoped polymers with IPES and UPS, respectively (for details, see Supplementary Fig.S2 and S3 and Table S1).

Fig. 2a and c show that all D-A polymers display a switch in the sign of α as the doping ratio of $FeCl_3$ increases to ≥ 0.67, while the homopolymers (P3HT and MEH-PPV) do not. The first polymer that we focus on is PDPP-4T (Fig. 2a and b), as it reaches the highest *n*-type and *p*-type PFs among all polymers investigated. At low doping concentrations, α is positive and decreases with increasing dopant concentration. Similarly, σ increases with increasing dopant concentration and plateaus at 16-17 S cm^{-1} at doping ratios of 0.25 to 0.67. The UV-Vis-NIR spectra presented in Supplementary Fig. S3b show that the neutral state absorbance continues to bleach while the polaron and bipolaron absorbance increases throughout the entire doping range, indicating that PDPP-4T continues to undergo further doping even at high dopant concentrations. Over the doping region where σ plateaus, α continues to steadily decrease as it moves from 69 to 22 μV K^{-1} and flips its sign to reach -74 μV K^{-1}. As a result, the PF changes from a maximum

of 25 μW m^{-1} K^{-2} when α is positive to a maximum of 9.2 μW m^{-1} K^{-2} when α is negative. This CP thereby shows both high *p*-type and high *n*-type PFs when only the dopant concentration is varied (see Supplementary Table S2 for a comparison of *n*-type polymers).

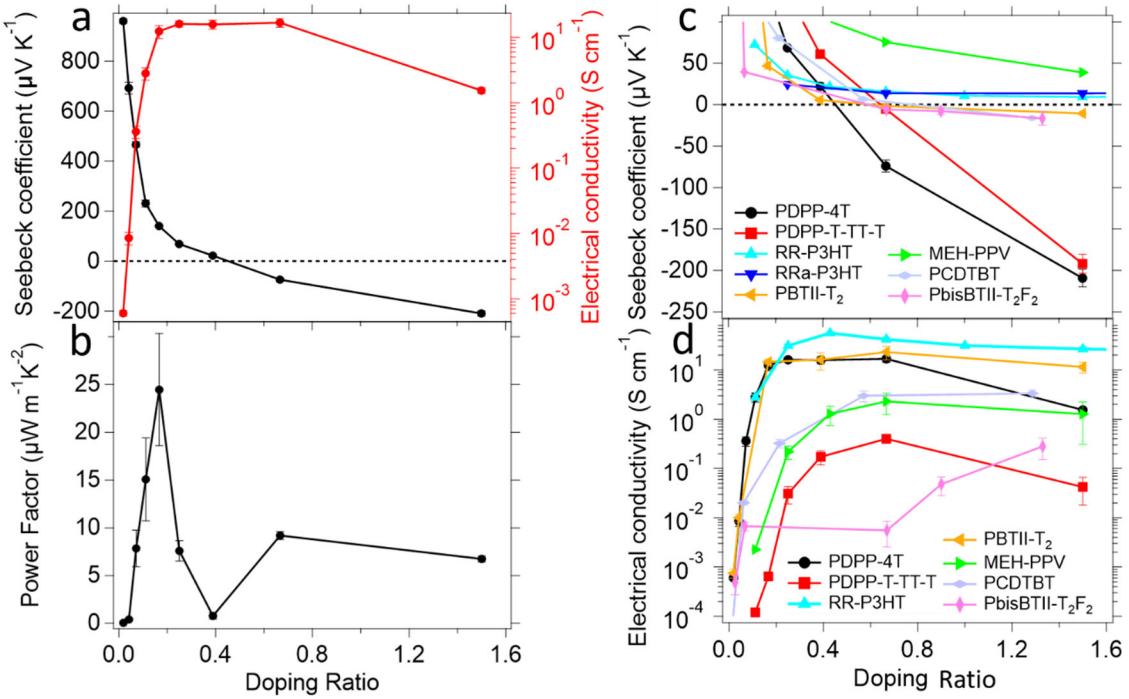

Fig. 2. Seebeck coefficient and electrical conductivity data for the CPs shown in Fig. 1 with varying $FeCl_3$ doping ratios. Seebeck coefficient (**a**), electrical conductivity (**a**), and power factor (**b**) for PDPP-4T, and Seebeck coefficients (**c**) and electrical conductivities (**d**) for all CPs investigated. Error bars are equal to ± one standard deviation from three to six individual samples measured for each doping ratio.

Fundamentally, and for the future design of CPs, it is important to identify why α changes sign. The Seebeck effect originates from the entropically driven diffusion of charge carriers and α can be defined by Equation 1 and Supplementary Equation S1.[25]

These equations apply regardless of the charge-carrier transport mechanism, material morphology, or material type.[9, 25]

$$\alpha = -\frac{k}{q}\int\left(\frac{E-E_F}{kT}\right)\frac{\sigma(E)}{\sigma}dE \qquad \text{Equation 1.}$$

Here, $\sigma(E)$ is affected by the DOS distribution, the Fermi distribution function, and the mobility of charge carriers at different energies, as further discussed in Supplemental Discussion S1. Defining the transport energy (E_T) as the average energy of charge carriers weighted by their contribution to the total electrical conductivity, $E_T = \int E\frac{\sigma(E)}{\sigma}dE$, if E_T lies above (below) E_F then α is negative (positive), as illustrated in Supplementary Fig. S4. In a metal, due to the large number of mobile electrons near E_F, the sign of α is often determined by the sign of $d\sigma/dE$ at E_F.[26] Notably, many metals with electrons as the charge carriers display positive α.[27] In doped semiconductors the sign of α normally depends on the sign of the charge carrier, with positive and negative α for *p*- and *n*-doped materials, respectively. This trend is because E_T is typically above E_F in an *n*-doped material and below E_F in a *p*-doped material. However, α may change sign at high doping levels in a semiconductor if E_F is pushed far enough into a band of states such that a metallic DOS appears or if the addition of a chemical dopant significantly alters the DOS distribution (e.g., as can occur in CPs).[20, 21]

The formation of new mobile states upon doping, specifically charge-transfer complexes with localized character lying at energies below E_F, was previously offered as an explanation for the change in the sign of α in *n*-doped PNDI2TEG-2T (see Supplementary Fig. S1 for polymer structures).[21] On the other hand, the change in the sign of α for *n*-

doped P(PymPh) was attributed to significant filling of the LUMO band,[20] essentially considering the heavily doped material as a metal (or Fermi glass) where E_F sits near the middle of a band of electronic states.[9] In both examples, the DOS and its relationship to E_F is critical. Thus, to probe the change in the energies of the occupied and unoccupied states relative to E_F we performed UPS and IPES measurements on PDPP-4T as a function of $FeCl_3$ loading.

The UPS and IPES data in Fig. 3 reveal that the transport gap narrows and eventually vanishes as doping increases. The undoped sample appears as expected, with E_F falling approximately halfway between the occupied (or HOMO) and unoccupied (or LUMO) bands and a 1.50 eV transport gap. As the doping concentration increases to 0.05, E_F moves closer to the HOMO onset, both the IE and EA increase slightly, and the transport gap is reduced to 1.30 eV. At 0.10 doping ratio the work function, IE, and EA increase and the transport gap further narrows. Notably, the increase in IE supports the recently updated model of energetics in doped CPs.[28-30] For the 0.10 doped sample, the transport gap reduces to 0.70 eV based on a linear fit to the lower third of the main onset regions. However, a tail of states in the IPES spectrum extends nearly to E_F, and accounting for this tail reduces the transport gap to only 0.40 eV. The doping ratio of 0.67 leads to a more pronounced signal in the IPES tail region that extends to E_F and a reduced transport gap of < 0.10 eV. This series of UPS and IPES spectra indicate that the DOS significantly changes upon doping, as opposed to E_F simply pushing into the band of occupied states. Here, the IPES and UPS spectra are most consistent with a semi-metallic DOS at high doping ratios. The convergence of the DOS is not unique to PDPP-4T, as UPS and IPES spectra of RR-P3HT

and PCDTBT at $FeCl_3$ doping ratios ≥ 0.43, as shown in Supplementary Fig. S5, reveal the same trends. Additional UPS and IPES measurements conducted on $NOBF_4$ doped PDPP-4T show a similar convergence of the DOS, indicating that these new states are largely from the polymer and not $FeCl_3$ (Supplementary Fig. S6 and Discussion S2).

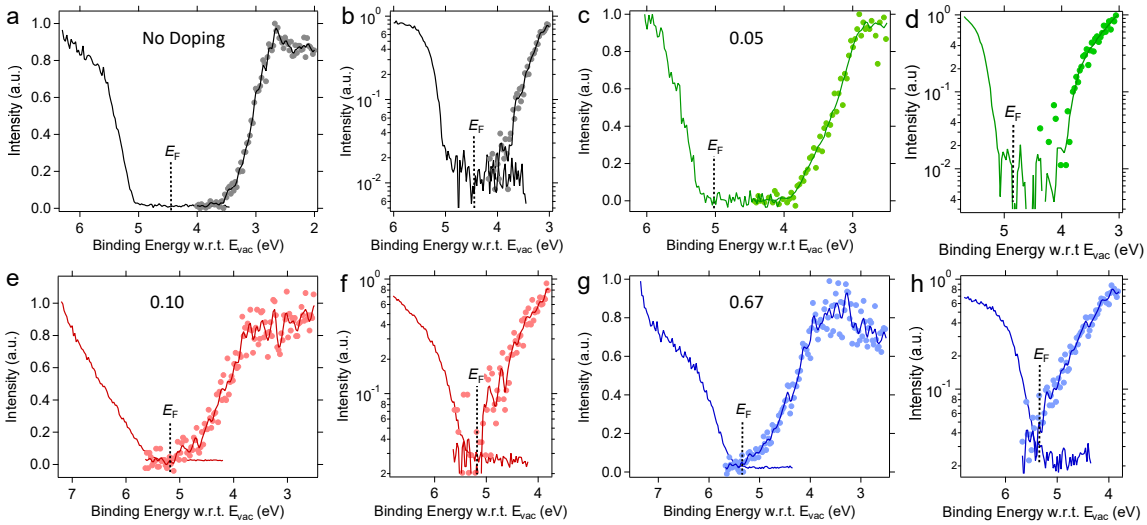

Fig. 3: Combined UPS and IPES spectra of PDPP-4T polymer films doped with $FeCl_3$ at varying ratios. Doping ratios (defined as the molar ratio of $FeCl_3$ dopant molecules to aromatic rings from the polymer) of 0 (**a** and **b**), 0.05 (**c** and **d**), 0.10 (**e** and **f**), and 0.67 (**g** and **h**) are displayed. Panels **b**, **d**, **f** and **h** have intensity on a logarithmic scale. IPES data is shown with dots indicating each data point and solid lines indicating a fit to the data using binomial smoothing. The UPS data (solid lines primarily at energies greater than E_F) is not smoothed. The work functions of the samples are 4.44, 5.02, 5.20, and 5.35 eV for the samples with doping ratios of 0, 0.05, 0.10, and 0.67, respectively. The IPES detector filter energy for undoped PDPP-4T is 4.40 eV, 4.88 eV for the 0.05 dopant ratio, and 5.80 eV for the 0.10 and 0.67 ratios. It is clear from these measurements that the transport gap shrinks with increasing concentration of the $FeCl_3$ *p*-dopant.

To investigate the nature of the charge carriers, we turn to Hall effect measurements, which can reveal the sign of the dominant mobile charge carriers undergoing band-like transport (see Supplemental Discussion S3 for a discussion of band-like transport). The Hall effect studies were performed with a sensitive *ac*-Hall method.[31, 32] Here, the negative or positive in-phase component of the Hall voltage corresponds to electrons or holes, respectively, as verified by control measurements of pristine rubrene single-crystal OFETs known to operate as *p*-type FETs[33] and commercially available *n*-doped Si wafers (Fig. 4). A $V_{Hall} > 0$ would indicate that holes are the dominant delocalized charge carriers and would be most consistent with a metallic DOS with E_F pushed into the band of occupied states. On the other hand, $V_{Hall} < 0$ would indicate that delocalized electrons are present, which would be consistent with a semi-metallic DOS with electrons moving through the unoccupied manifold of states. Fig. 4 indeed shows that both PDPP-4T and RR-P3HT that are moderately to highly *p*-doped with $FeCl_3$ show a negative Hall voltage, indicating electrons are the dominant band-like (i.e., delocalized) charge carriers. The *n*-type Hall effect in PDPP-4T heavily doped with $FeCl_3$ at 0.67 doping ratio is consistent with the negative α; however, PDPP-4T with a lower doping ratio of 0.10 and RR-P3HT with 0.10 and 0.67 doping ratios also show an *n*-type Hall effect (Fig. 4 and Supplementary Fig. S8) even though α is positive. We note that segregation of $FeCl_3$ into clusters, with preferential electron transport through such phases, can be excluded from the possible mechanisms of the observed electron conduction (see Supplemental Discussion S5 for a discussion of control experiments). Additional discussion of the Hall effect data can be found in Supplemental Discussion S4.

To rationalize the Hall effect and α data, one must keep in mind that: (a) the motion of electrons and holes may be governed by different mechanisms, such as hopping or band-like transport, and (b) while both hopping and band-like carriers contribute to the Seebeck effect, only the band-like carriers experience the classic Lorentz force and contribute to the Hall effect. We therefore propose that the negative Hall voltages observed for the PDPP-4T and RR-P3HT samples with positive α can be explained by the primary sensitivity of the Hall effect to delocalized charge carriers with more band-like character.[32] For samples with doping ratios < 0.10, hopping-type transport of holes is dominant, leading to positive α and an indiscernible Hall effect (Supplementary Fig. S8). For doping ratios $\geq$ 0.10, the contribution of holes diminishes while that of delocalized electrons increases. Notably, on the scale of the thin film the transport is not band-like, as temperature dependent σ measurements (Supplementary Fig. S9) of both PDPP-4T and RR-P3HT fit well with models of hopping-type transport.[10] Thus, the band-like transport revealed by the Hall effect measurements likely occurs over tens of nanometers in crystalline regions and is disrupted by amorphous regions. Building upon early work with PANI,[3, 4, 16, 17] our α and Hall effect measurements provide direct experimental evidence for the presence of both positive and negative charge carriers that move through different transport mechanisms in *p*-doped CPs.

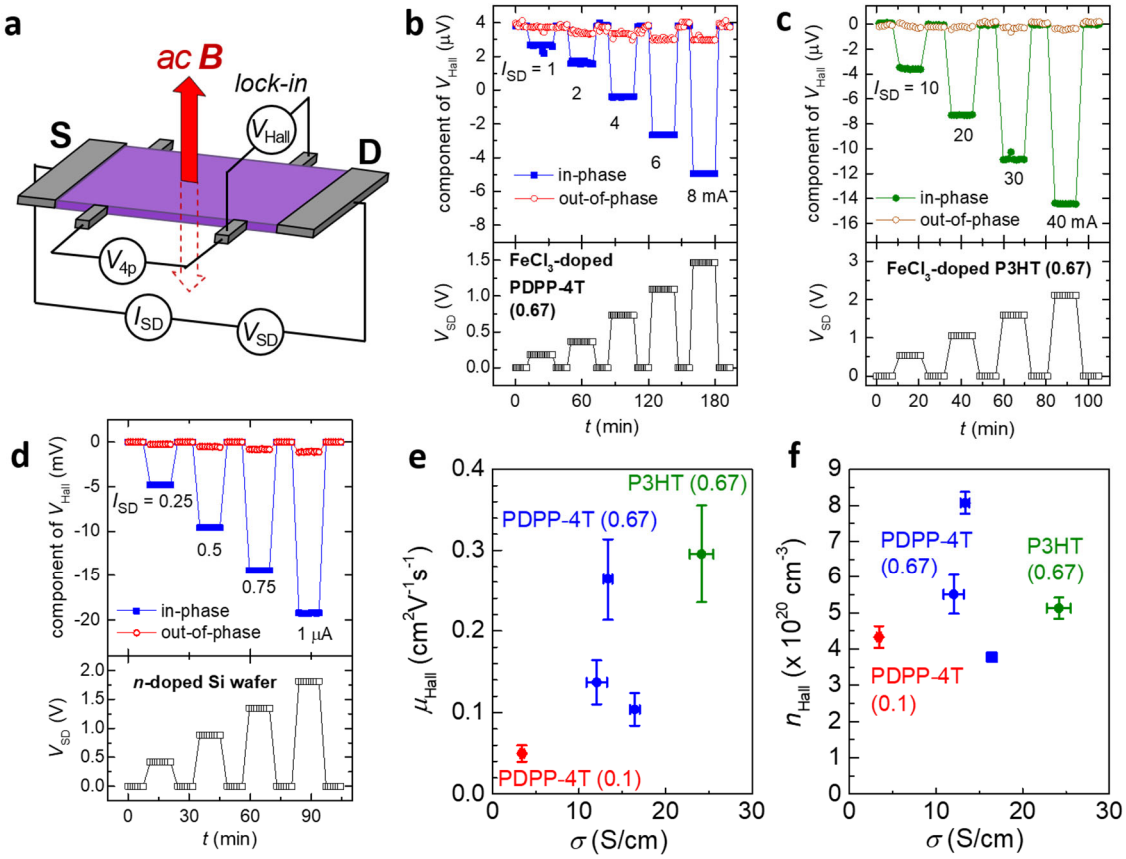

Fig. 4. *ac*-Hall effect measurements of CP films heavily doped with $FeCl_3$. (**a**) Schematics of *ac*-Hall effect measurements using an *ac* magnetic field, *B*, oscillating at a frequency f = 0.7 – 0.8 Hz, and an *ac* Hall voltage, V_{Hall}, detected by a lock-in amplifier, while a longitudinal *dc* current, I_{SD}, flows between the source (S) and drain (D) contacts. The Hall data for $FeCl_3$-doped PDPP-4T (**b**) and $FeCl_3$-doped RR-P3HT (**c**) with doping ratios of 0.67. (**d**) Control *ac*-Hall measurements of an *n*-doped Si wafer to verify the carrier sign assignment. The in-phase and out-of-phase components of V_{Hall}, with the corresponding I_{SD} values indicated, are shown in the upper panels. The source-drain voltage, V_{SD}, corresponding to different I_{SD}, are shown in the lower panels. The "ups" and "downs" in the V_{Hall} signal are due to I_{SD} being switched on and off to establish the zero-current

baseline of the Hall voltage. The resultant Hall mobility vs. conductivity (**e**) and Hall carrier density vs. conductivity (**f**) for a collection of all measured polymer samples (each data point is an average of at least four measurements on one sample). Note: n_{Hall} and σ are the 3D values obtained from the corresponding measured 2D (projected) values by dividing them by the film thickness. (**e** and **f**) Error bars are based on the standard error in film thickness measurements and the standard deviation in values extracted from the Hall effect measurements at differing currents. The main observation is the negative sign of the in-phase Hall voltage (relative to the zero-current background) in CPs heavily doped with an oxidizing dopant ($FeCl_3$), signaling an electron dominant charge transport.

Quantitative EPR measurements were conducted on PDPP-4T and RR-P3HT films doped with $NOBF_4$ to provide additional insight into the nature of the charge carriers, including whether unpaired (polarons) or paired (bipolarons) electron spin states were created through doping and the quantity of unpaired electrons (spins), as shown in Fig. 5a and Supplementary Fig. S10. The dopant $NOBF_4$ was used in place of $FeCl_3$ to eliminate interference and line broadening from $FeCl_3$.[34] As the $NOBF_4$ doping ratio increases from 0.015 to 0.10 the spin concentration increases steadily from 9.4×10^{18} to 5.1×10^{19} spins cm^{-3}, as shown in Fig. 5a. Following this initial rapid increase, the spin concentration remains constant as the doping ratio increases from 0.10 to 0.40 and increases by *ca.* 30% as the doping ratio increases further to 0.67. This relatively small increase in spin concentration between 0.10 and 0.67 doping ratios, combined with the five-fold decrease in the neutral state UV-Vis-NIR absorbance over this doping region (Supplementary Fig. S3c), indicates that primarily bipolarons are forming beyond a doping ratio of 0.10. At 0.67 doping ratio

the spin concentration is 6.7×10^{19} spins cm^{-3}, which corresponds with 1.9% of a spin per aromatic ring in the sample. This amount of spin per aromatic ring is similar to PEDOT:PSS, where values range from 0 to 2.3%, and the dominant charge-carriers are bipolarons.[9] EPR peak broadening (Supplementary Fig. S10b) supports that the unpaired electrons continuously become more delocalized as the doping ratio increases to 0.10 and beyond.[15, 35] These trends are not unique to PDPP-4T, as RR-P3HT shows similar changes in spin concentration and peak broadening with increasing doping ratios (Fig. 5a and Supplementary Fig. S10d). Interestingly, RR-P3HT displays a lower maximum spin concentration than PDPP-4T and does not show the increase in spin concentration between 0.40 and 0.67 doping ratios that PDPP-4T does. It is possible that the additional unpaired electrons appearing in PDPP-4T between 0.40 and 0.67 doping ratios, which are absent in RR-P3HT, play a role in influencing the sign change of α.

Combining the EPR, UPS, IPES, UV-Vis-NIR, and Hall effect measurements with DFT calculations we present a picture of how the electronic states vary as a function of doping concentration, as shown in Fig. 5b-f. At low doping concentrations, Coulomb interactions increase the IE and EA and the now singly spin occupied and unoccupied spatial orbitals are split.[28-30] These trends are shown by DFT-derived frontier molecular orbital energies for neutral and singly charged oligomers of five different systems studied here (Supplementary Table S4 and S5). Beyond this low-doping regime we turn primarily to experimental data, as accurate DFT calculations of electronic states at high doping concentrations requires further development and validation.[30, 36]

The DOS and charge-carrier distribution schematics shown in Fig. 5b-f are supported by (i) EPR results that show bipolarons begin to form and more delocalized unpaired electronic states appear at higher doping ratios, (ii) UPS and IPES results that show both the IE and EA continue to increase while the transport gap narrows, and (iii) Hall effect measurements that show electrons become the dominant delocalized charge carriers. Conceptually, we consider these electrons as moving within a delocalized band in the crystalline regions, as shown in Fig. 5e and f. Concurrently, positively charged carriers that display more localized character are present in the amorphous regions. The more localized nature of these charged carriers is supported by the hopping-type transport observed in the temperature dependent σ measurements, while the observation of positive α (even when negative Hall voltages are detected) combined with the oxidizing nature of $FeCl_3$ supports their positive polarity. Temperature dependent α measurements further support that both hopping and semi-metallic charge carriers are present, as discussed in Supplemental Discussion S6 and presented in Supplementary Fig. S12 and S13.

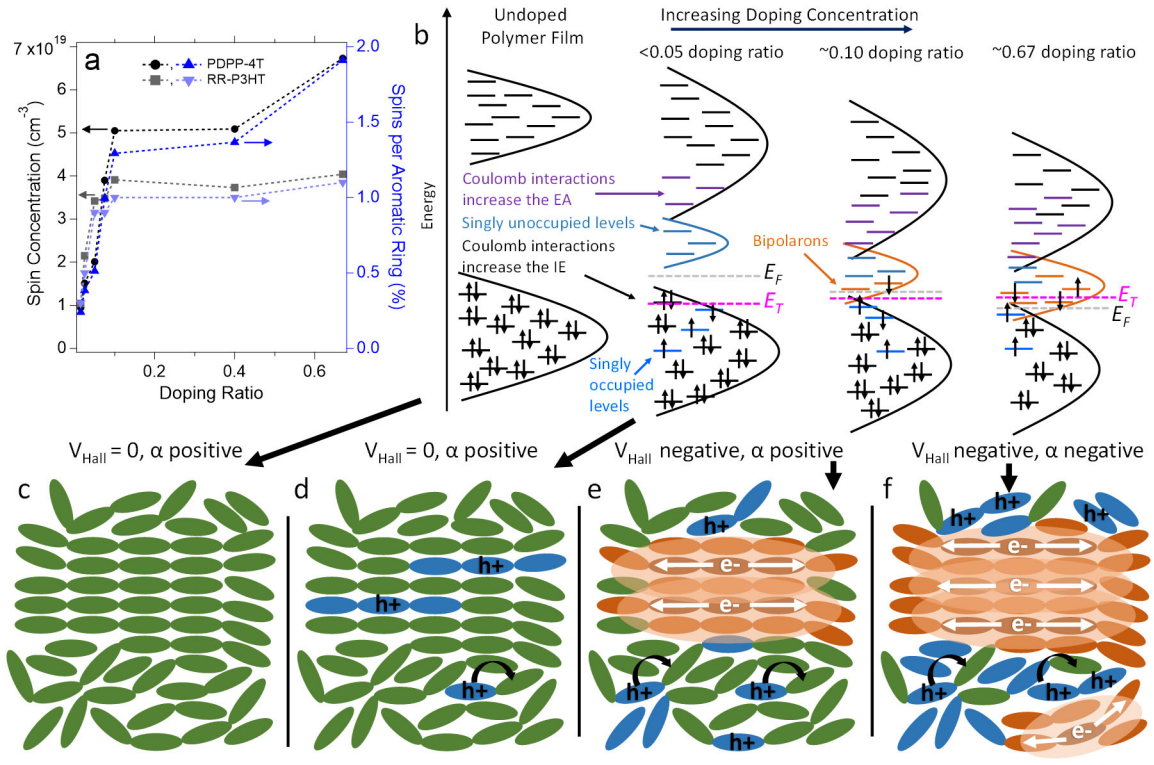

Fig. 5. Quantitative spin concentrations and schematics depicting the density of states and charge-carrier transport in CPs as a function of $FeCl_3$ or $NOBF_4$ doping ratio. **(a)** Spin concentrations as determined by EPR for $NOBF_4$ doped PDPP-4T and RR-P3HT. **(b)** Density of states schematic highlighting how Coulomb interactions, spin orbital splitting, and bipolaron formation result in the narrowing of the transport gap and a shift in the transport energy (E_T) from below the Fermi energy (E_F) to above E_F. In **(b)** black arrows represent electrons, gray and pink dashed lines indicate the positions of E_F and E_T, respectively, the blue parabola indicates the distribution of unoccupied spin orbitals and orange parabolas indicate the band composed of bipolarons and unoccupied spin orbitals. **(c-f)** Schematics illustrating transport in CPs with varying doping levels. In **(c-f)** green ovals represent neutral polymer segments, blue ovals represent polymer segments with polaron character, orange ovals represent polymer segments with bipolaron character, h^+ indicates a hole

from a polaron, e^- indicates delocalized electrons in the bipolaron band, curved black arrows indicate hopping type transport, and white arrows indicate more band-like transport occurring in the ordered regions.

An important question remaining is what determines whether a CP will display a sign change in α? Influential factors likely include the size and structure of the dopant (for example, RR-P3HT doped with F4TCNQ shows positive Hall voltages,[37] as does electrochemically doped RR-P3HT with TFSI as a counterion),[10] polymer structure, crystalline packing,[38] morphology, and dopant distribution. The presence of negative charge carriers in the crystalline regions alone does not necessarily imply a negative α. Rather, it is the balance between contributions from charge carriers in the amorphous and crystalline regions that ultimately determines the sign of α when both carrier types are present. Thus, in considering whether a CP will show a change in the sign of α, the relative energies of electronic states in the amorphous and crystalline regions must be considered along with the charge-carrier mobilities in both phases (see Supplemental Discussion S1 for more details).

This work highlights the potential of doping CPs with strong electron acceptors to achieve high-performing *p*- and *n*-type thermoelectrics, both realized in the same CP/dopant system by varying only the concentration of the dopant. Through this approach, traditionally viewed *p*-type CPs with EAs that make *n*-type doping difficult can now be investigated for *n*-type thermoelectric materials through heavy *p*-type doping. This strategy thereby significantly enriches the potential library of *n*-type CPs for

thermoelectric applications. Several CPs demonstrate a change in the sign of the Seebeck coefficient from positive to negative, thus showing the generality of this approach. Fundamentally, our work builds upon work from the 1980s and 1990s, where positive and negative α were observed in PANI. Here, our combined Hall and Seebeck measurements provide direct evidence that both holes and electrons contribute significantly to α, with the positive and negative charge carriers displaying hopping and band-like transport, respectively. The UPS and IPES measurements show that the occupied and unoccupied states converge upon heavy doping in the CPs examined, leading to a diminishing transport gap and a semi-metallic DOS. As a result, the sign of α is determined by the balance between electron and hole conduction.

References

1. Bolto, B., McNeill, R., Weiss, D. Electronic Conduction in Polymers. III. Electronic Properties of Polypyrrole. *Aust. J. Chem.*, **16,** 1090-1103 (1963).
2. Chiang, C. K., Fincher, C. R., Park, Y. W., Heeger, A. J., Shirakawa, H., Louis, E. J.*, et al.* Electrical Conductivity in Doped Polyacetylene. *Phys. Rev. Lett.*, **39,** 1098-1101 (1977).
3. Joo, J., Long, S. M., Pouget, J. P., Oh, E. J., MacDiarmid, A. G., Epstein, A. J. Charge transport of the mesoscopic metallic state in partially crystalline polyanilines. *Phys. Rev. B*, **57,** 9567-9580 (1998).
4. Mateeva, N., Niculescu, H., Schlenoff, J., Testardi, L. R. Correlation of Seebeck coefficient and electric conductivity in polyaniline and polypyrrole. *J. Appl. Phys.*, **83,** 3111-3117 (1998).
5. Shirakawa, H., Louis, E. J., MacDiarmid, A. G., Chiang, C. K., Heeger A. J. Synthesis of electrically conducting organic polymers: halogen derivatives of polyacetylene, (CH). *J. Chem. Soc., Chem. Commun.* 578-580 (1977).
6. Park, Y. W., Lee, Y. S., Park, C., Shacklette, L. W., Baughman, R. H. Thermopower and conductivity of metallic polyaniline. *Solid State Commun.*, **63,** 1063-1066 (1987).
7. Wang, Z. H., Li, C., Scherr, E. M., MacDiarmid, A. G., Epstein, A. J. Three dimensionality of ''metallic'' states in conducting polymers: Polyaniline. *Phys. Rev. Lett.*, **66,** 1745-1748 (1991).
8. Lee, K., Cho S., Heum, Park S., Heeger, A. J., Lee, C.-W., Lee, S.-H. Metallic transport in polyaniline. *Nature*, **441,** 65-68 (2006).
9. Bubnova, O., Khan, Z. U., Wang, H., Braun, S., Evans, D. R., Fabretto, M.*, et al.* Semi-metallic polymers. *Nat. Mater.*, **13,** 190 (2013).
10. Wang, S., Ha, M., Manno, M., Daniel, Frisbie C., Leighton, C. Hopping transport and the Hall effect near the insulator–metal transition in electrochemically gated poly(3-hexylthiophene) transistors. *Nat. Commun.*, **3,** 1210 (2012).

11. Chance, R. R., Brédas, J. L., Silbey, R. Bipolaron transport in doped conjugated polymers. *Phys. Rev. B*, **29,** 4491-4495 (1984).
12. Zuppiroli, L., Bussac, M. N., Paschen, S., Chauvet, O., Forro, L. Hopping in disordered conducting polymers. *Phys. Rev. B*, **50,** 5196-5203 (1994).
13. Yoon, C. O., Reghu, M., Moses, D., Heeger, A. J., Cao, Y., Chen, T. A*., et al.* Hopping transport in doped conducting polymers in the insulating regime near the metal-insulator boundary: polypyrrole, polyaniline and polyalkylthiophenes. *Synth. Met.*, **75,** 229-239 (1995).
14. Zuo, F., Angelopoulos, M., MacDiarmid, A. G., Epstein, A. J. Transport studies of protonated emeraldine polymer: A granular polymeric metal system. *Phys. Rev. B*, **36,** 3475-3478 (1987).
15. Tanaka, H., Kanahashi, K., Takekoshi, N., Mada, H., Ito, H., Shimoi, Y*., et al.* Thermoelectric properties of a semicrystalline polymer doped beyond the insulator-to-metal transition by electrolyte gating. *Sci. Adv.*, **6,** eaay8065 (2020).
16. Hundley, M. F., Adams, P. N., Mattes, B. R. The influence of 2-acrylamido-2-methyl-1-propanesulfonic acid (AMPSA) additive concentration and stretch orientation on electronic transport in AMPSA-modified polyaniline films prepared from an acid solvent mixture. *Synth. Met.*, **129,** 291-297 (2002).
17. Holland, E. R., Monkman, A. P. Thermoelectric power measurements in highly conductive stretch-oriented polyaniline films. *Synth. Met.*, **74,** 75-79 (1995).
18. Thomas, E. M., Popere, B. C., Fang, H., Chabinyc, M. L., Segalman, R. A. Role of Disorder Induced by Doping on the Thermoelectric Properties of Semiconducting Polymers. *Chem. Mater.*, **30,** 2965-2972 (2018).
19. Venkateshvaran, D., Nikolka, M., Sadhanala, A., Lemaur, V., Zelazny, M., Kepa, M*., et al.* Approaching disorder-free transport in high-mobility conjugated polymers. *Nature*, **515,** 384-388 (2014).
20. Hwang, S., Potscavage, W. J., Yang ,Y. S., Park, I. S., Matsushima, T., Adachi, C. Solution-processed organic thermoelectric materials exhibiting doping-concentration-dependent polarity. *PCCP*, **18,** 29199-29207 (2016).
21. Liu, J., Ye, G., Zee, B. v. d., Dong, J., Qiu, X., Liu, Y*., et al.* N-Type Organic Thermoelectrics of Donor–Acceptor Copolymers: Improved Power Factor by Molecular Tailoring of the Density of States. *Adv. Mater.*, **30,** 1804290 (2018).
22. Yoon, C. O., Reghu, M., Moses, D., Cao, Y., Heeger, A. J. Thermoelectric power of doped polyaniline near the metal-insulator transition. *Synth. Met.*, **69,** 273-274 (1995).
23. Brault, D., Lepinoy, M., Limelette, P., Schmaltz, B., Van, F. T. Electrical transport crossovers and thermopower in doped polyaniline conducting polymer. *J. Appl. Phys.*, **122,** 225104 (2017).
24. Liang, Z., Zhang, Y., Souri, M., Luo, X., Boehm, A. M., Li, R*., et al.* Influence of dopant size and electron affinity on the electrical conductivity and thermoelectric properties of a series of conjugated polymers. *J. Mater. Chem. A*, **6,** 16495-16505 (2018).
25. Fritzsche, H. A general expression for the thermoelectric power. *Solid State Commun.*, **9,** 1813-1815 (1971).
26. Xu, B., Verstraete, M. J. First Principles Explanation of the Positive Seebeck Coefficient of Lithium. *Phys. Rev. Lett.*, **112,** 196603 (2014).
27. Rowe, D. M. *CRC Handbook of Thermoelectrics*. CRC Press, 1995.
28. Winkler, S., Amsalem, P., Frisch, J., Oehzelt, M., Heimel, G., Koch, N. Probing the energy levels in hole-doped molecular semiconductors. *Mater. Horiz*, **2,** 427-433 (2015).
29. Png, R.-Q., Ang, M. C. Y., Teo, M.-H., Choo, K.-K., Tang, C. G., Belaineh, D*., et al.* Madelung and Hubbard interactions in polaron band model of doped organic semiconductors. *Nat. Commun.*, **7,** 11948 (2016).

30. Heimel, G. The Optical Signature of Charges in Conjugated Polymers. *ACS Cent. Sci.*, **2,** 309-315 (2016).
31. Chen, Y., Yi, H. T., Podzorov, V. High-Resolution *ac* Measurements of the Hall Effect in Organic Field-Effect Transistors. *Phys. Rev. Appl.*, **5,** 034008 (2016).
32. Yi, H. T., Gartstein, Y. N., Podzorov, V. Charge carrier coherence and Hall effect in organic semiconductors. *Sci. Rep.*, **6,** 23650 (2016).
33. Podzorov, V., Menard, E., Rogers, J. A., Gershenson, M. E. Hall Effect in the Accumulation Layers on the Surface of Organic Semiconductors. *Phys. Rev. Lett.*, **95,** 226601 (2005).
34. Houzé, E., Nechtschein, M., Pron A. Fixed-spin-induced ESR linewidth and polaron mobility in conducting polymers. *Phys. Rev. B*, **56,** 12263-12267 (1997).
35. Elliott, R. J. Theory of the Effect of Spin-Orbit Coupling on Magnetic Resonance in Some Semiconductors. *Phys. Rev.*, **96,** 266-279 (1954).
36. Zozoulenko, I., Singh, A., Singh, S. K., Gueskine, V., Crispin, X., Berggren, M. Polarons, Bipolarons, And Absorption Spectroscopy of PEDOT. *ACS Appl. Polym. Mater.*, **1,** 83-94 (2019).
37. Scholes, D. T., Yee, P. Y., Lindemuth, J. R., Kang, H., Onorato, J., Ghosh, R.*, et al.* The Effects of Crystallinity on Charge Transport and the Structure of Sequentially Processed F4TCNQ-Doped Conjugated Polymer Films. *Adv. Funct. Mater.*, **27,** 1702654 (2017).
38. Jacobs, I. E., Cendra, C., Harrelson, T. F., Bedolla Valdez, Z. I., Faller, R., Salleo, A.*, et al.* Polymorphism controls the degree of charge transfer in a molecularly doped semiconducting polymer. *Mater. Horiz.*, **5,** 655-660 (2018).

Methods

Materials. RR-P3HT and RRa-P3HT (Rieke metals); iron (III) chloride (anhydrous, 98%, crystalline, Alfa Aesar); chloroform (Anhydrous, stabilized with 1% ethanol, DriSolv); acetonitrile (>99.5%, Sigma-Aldrich); MEH-PPV (M_n 40,000-70,000, Sigma-Aldrich), PCDTBT (M_n 100,000-140,000, Sigma-Aldrich); $NOBF_4$ (98%, Alfa Aesar) and bismuth metal (99.99%, Kurt J.Lesker) were purchased from the indicated suppliers and used as received. PDPP-4T, PDPP-T-TT-T, PBTII-T_2, and PbisBTII-T_2F_2 were synthesized following previous references.[39-41]

Solution preparation. All solution preparation and film casting were conducted in a nitrogen filled glovebox with H_2O and O_2 typically < 0.1 ppm. RR-P3HT and RRa-P3HT were dissolved in chloroform (10 mg mL^{-1}); PDPP-4T, PDPP-T-TT-T, MEH-PPV, PCDTBT, PBTII-T_2 and PbisBTII-T_2F_2 were prepared at 5 mg mL^{-1} in chloroform; $FeCl_3$ was prepared in chloroform at 10 mg mL^{-1}; $NOBF_4$ was prepared in acetonitrile at 2.5 mg mL^{-1}. Solutions of the polymer and dopant were formed through mixing the pure polymer solution with the dopant solution at varying concentrations. For $NOBF_4$ doped samples, $NOBF_4$ solution was used for doping ratios < 0.16, and $NOBF_4$ solid was used for doping ratios > 0.16. The dopant ratio corresponds to the molar ratio of dopant molecules to aromatic rings from the polymer. The moles of aromatic rings from the polymer were determined by calculating the molar mass of the polymer repeat unit and dividing by the number of aromatic rings to determine the molar mass per aromatic ring. Fused rings, such as the DPP unit, were counted as two aromatic rings. The doped solutions were stirred on a hotplate at 40 °C for 10 hours. Films were fabricated by drop-casting onto cleaned glass substrates. Film thicknesses ranged from 2 to 4 μm.

UPS and IPES. UPS measurements were carried out in a PHI 5600 UHV system with an 11-inch diameter hemispherical electron energy analyzer with multichannel detector. The photon source for the UPS measurements was an Excitech H Lyman-α lamp (E-LUX^{TM}121, 10.2 eV emission) coupled with a 90^{o} ellipsoidal mirror (E-LUX^{TM} EEM Optical Module) with a dry oxygen purge of the beam path at 7 - 9 Torr, as detailed in a previous publication.[42] Negative 5 V bias was applied to all samples during UPS measurements and the measurements were conducted with a pass energy of 5 eV. IPES measurements were collected in Bremsstrahlung isochromat mode with electron kinetic energies below 5 eV to minimize sample damage. The low energy electron beam was generated using a Kimball Physics ELG-2 electron gun equipped with a low temperature (1150 K) BaO cathode. Emitted photons were collected and focused with a fused silica bi-convex lens into the photon detector that consisted of an optical bandpass filter (214 nm, Andover corporation, 254 nm or 280 nm, Semrock) and a photomultipler tube (R585, Hamamatsu Photonics). External light was completely blocked from the IPES system during all IPES measurements and the samples were biased at -20 V during measurement.[24]

Sheet resistance. Sheet resistance was measured with a four-point probe setup (Signatone S302-4, Keithley 2450 source meter); film thicknesses were measured with a Dektak D6M/32 profilometer.

Seebeck coefficient measurement. A custom-built setup was used to check the Seebeck coefficient, as detailed in our previous report.[43] 100 nm bismuth (calibrated α = -62.1±2.6 μV K^{-1}) and 100 nm of gold, for serving as a standard to monitor the temperature difference and to serve as electrodes and electrical contact pads, respectively, were thermally evaporated at <1x10^{-6} Torr. Examples of sample measurements are shown in Fig. S11. Error bars in the Seebeck coefficients are calculated based on the standard deviation in the measured Seebeck coefficients of three to six individual samples.

UV-Vis-NIR absorbance measurement. Samples for UV-Vis-NIR absorbance were prepared by spin casting 75 μL of 5 mg mL^{-1} doped CP solutions on glass (for 350-1800 nm measurements) or sapphire (for 300-3300 nm measurements) substrates with 1000 rpm spin speed for 30 seconds in an N_2 filled glovebox. 350-1800 nm UV-vis-NIR spectra were measured with an Agilent Technologies Cary 6000i UV-Vis-NIR spectrophotometer at room temperature; 300-3300 nm UV-Vis-NIR spectra were measured with an Agilent Technologies Cary 5000 UV-Vis-NIR spectrophotometer at room temperature. The 300-3300 nm scans were conducted with the sample under a nitrogen purge with a scan rate of 600 nm min^{-1} at room temperature. The baseline was collected with a blank glass or sapphire substrate.

Hall effect measurement. Samples for Hall effect measurements were prepared in the Graham laboratory at UK and shipped overnight in nitrogen sealed pouches to the Podzorov group at Rutgers for testing. In the *ac*-Hall effect measurements, a low-frequency (< 1.5 Hz) *ac* magnetic field of a small magnitude (r.m.s. B = 0.23 T), applied perpendicular to the film's plane, is used in combination with a phase-sensitive detection of the corresponding *ac*-Hall voltage, V_{Hall}, by a lock-in amplifier, while a longitudinal source-drain excitation *dc*-current, I_{SD}, is applied to the film (Fig. 4 of the main text). All electric measurements were carried out at room temperature in a coarse vacuum (10^{-2} Torr). Keithley K6221 current source, Hewlett-Packard HP34401A multimeter and Keithley K6514 electrometer were used to set the source-drain current, I_{SD}, measure the source-drain voltage, V_{SD}, and monitor the four-probe voltage, V_{4p}, respectively. In the four-probe

conductivity measurements, I_{SD} flows between the source and drain contacts, while V_{SD} and V_{4p} are measured between the source and drain contacts and the voltage probes along the conducting channel, respectively (Fig. 4 of the main text).[44, 45] This allows comparing the contact-resistance corrected (that is, the four-probe) longitudinal conductivity of the doped polymer films, $\sigma_{4p} \equiv (D/W) \cdot (I_{SD}/V_{4p})$, with its two-probe conductivity, $\sigma_{2p} \equiv (L/W) \cdot (I_{SD}/V_{SD})$, where *D* is the center-to-center distance between the voltage probes along the channel, *W* is the channel width, and *L* is the channel length. We first verified that the doped polymer samples studied here were not contact limited by performing measurements of the longitudinal transport via the four-probe technique. In this work, we use the sheet conductivity (per square) in Siemens (1 S ≡ 1 Ω^{-1}) divided by the film thickness to calculate the electric conductivity in S cm^{-1}. In the *ac*-Hall measurements, the in-phase and out-of-phase components of the Hall voltage, V_{Hall}^{ip} and V_{Hall}^{op}, are registered by a Stanford Research SR830 lock-in amplifier tuned into the frequency of the *ac*-*B* field. The *ac*-*B* field is measured by a Gaussmeter that provides a reference signal for the lock-in. The net Hall voltage, V_{Hall}, is determined as the absolute value of a vector with the components V_{Hall}^{ip} and V_{Hall}^{op}: $V_{Hall} \equiv \sqrt{\left(V_{Hall}^{ip}\right)^2 + \left(V_{Hall}^{op}\right)^2}$, following the previously developed procedure.[31] The *ac*-*B* field is generated by a rotating assembly of permanent neodymium (Nd) magnets. In the polymer devices studied here, *L* = *W* = 1 mm, and *D* = 0.34mm. However, since the polymer films were unpatterned, the Hall mobility and carrier densities, μ_{Hall} and n_{Hall}, reported in the main text (Fig. 4 of the main text) should be taken as estimates, rather than precise values, merely for sample comparison.

Electron paramagnetic resonance (EPR). Samples were prepared for EPR measurements by drop casting doped polymer solutions in chloroform on clean microscope glass slides, scraping off the dried films, and loading them into EPR-grade quartz tubes in a nitrogen-filled glovebox (O_2 < 1ppm, H_2O < 1ppm). The dopant concentration was adjusted according to the previously mentioned details to reach the correct dopant ratio. The EPR tubes were sealed with PTFE tape, plastic caps, and wrapped with parafilm before moving out of the glovebox. All samples were checked within five hours after being made. Electron paramagnetic resonance (EPR) spectroscopy was performed at ambient temperature (~21 ^{o}C) on a Bruker EMXplus EPR spectrometer (Billerica, MA) with an X-band cavity. Non-doped polymer, pure dopant, and 2,2,6,6-tetramethyl-1-piperidinyloxy (TEMPO) were used as control samples. All EPR spectra for a given material that are presented on the same plot were obtained on a single day. The sample was placed into the cavity, the cavity was tuned using the WinEPR auto-tuning method, and EPR peaks were measured. Parameters for measuring the samples were microwave frequency 9.877 GHz; modulation frequency 100 kHz; time constant 40.96 ms; conversion time 42 ms; resolution 1024; center field 3524 G; modulation amplitude 1.0 G; receiver gain 6.32 x 10^2; sweep width 100 G; and microwave power of 2 or 0.02 mW. The g-value axis was calibrated relative to a crystalline 2,2-diphenyl-1-picrylhydrazine (DPPH) standard using Bruker WinEPR software. Analysis of EPR peaks was initially performed using Bruker WinEPR software and further analyzed in Igor Pro.

EPR measurements were initially conducted on samples with quantities ranging from 0.1 mg polymer to 3 mg of polymer. In the 3 mg samples, clear polymer saturation effects (i.e., artificial peak broadening, Q values <1000) were observed and led to inaccurate quantification of spin densities for samples with doping ratios above 0.05. For the higher doped samples (e.g., 0.40 doping ratio), <0.5 mg samples were necessary to avoid saturation effects. Notably, due to the delocalized nature of electrons in the CP samples, saturation effects are observed at much lower total spin quantities than observed for common EPR standards, such as TEMPO,[46] where the unpaired electrons are more localized. All measurements reported in the manuscript and SI use 0.2 mg of polymer, unless otherwise noted. EPR measurements

at varying powers were recorded to ensure that the microwave power used for the measurements did not result in artificial line broadening and was in the range where the signal intensity increased with the square root of the microwave power.

The spin density was quantified in $NOBF_4$ doped PDPP-4T and RR-P3HT samples through comparing the intensity of the double integral of the EPR spectra to a standard curve constructed from TEMPO in toluene and accounting for the quality factor (Q).[47] Briefly, two separate TEMPO calibration series were performed with the total number of TEMPO molecules in a 100 or 50 µL volume ranging from 1.0×10^{15} to 4.0×10^{17}. The double integral of the EPR spectra divided by Q, where Q is the quality factor of the EPR cavity when the sample of interest is present, was plotted vs. the number of spins in the sample to construct a calibration curve. Based on the standard deviation of the TEMPO calibration samples, the uncertainty in spin concentration is ±10%. To determine the spin concentration in the polymer samples, the total number of unpaired electrons was first calculated by comparing the double integral intensity/Q value to the calibration curve. The spin ratio per aromatic ring was determined by dividing the total number of spins by the total number of aromatic rings present in the sample. The total spin concentrations (i.e., spins cm^{-3}) in the samples were calculated based on the dopant and polymer mass in the samples combined with the dopant density (2.18 g cm^{-3} for $NOBF_4$) and polymer density (1.1 g cm^{-3}, assuming PDPP-4T and RR-P3HT have a similar density).[48] This calculated density does not account for the loss of NO, which may occur upon doping, and neglects changes in crystalline structure that may lead to additional density changes.

Density functional theory (DFT) calculations. Density functional theory (DFT) calculations were carried out on select oligomers to represent the polymers in the study using the Gaussian 16 (Rev. A.03) software suite.[49] Specifically, the DFT calculations were performed at the optimally tuned (OT)-LC-ωPBE/6-31G(d,p) level of theory;[50-55] the (OT)-LC-ωPBE functional was selected to avoid substantial multielectron self-interaction errors observed with many commonly used functionals. Omega tuning was performed via the iterative, nonempirical ionization potential (IP) tuning procedure.[56] Normal mode analyses were carried out for all optimized structures to ensure that the geometries were located in minima on the potential energy surface. We note that calculations were also carried out for higher oxidation states than those reported; however, due to the lack of Coulombic screening of like charges on the same oligomer from either the dopant counterion or the polarizable environment, we do not report these data.[57] Further, many of the higher oxidation states can have multiple spin multiplicities, and we note that not all of the optimized charge and spin states led to states that possessed no negative normal modes, *i.e.* the optimized geometries were transition states. We suspect that this could be an issue in using computational methods in exploring polymer/oligomer systems with high oxidation states and that the normal mode analyses need to be completed and reported.

Temperature dependent Seebeck coefficient measurements. The device structure for measuring temperature dependent Seebeck coefficients is shown in Fig. S12a. Glass substrates of 1”×1” size and 1 mm thickness were cut from 1”× 3” glass microscope slides (VWR) and were sequentially sonicated in aqueous detergent (sodium dodecyl sulfate, Sigma-Aldrich), deionized water, acetone, and 2-propanol (IPA) each for 15 minutes followed by 10 minutes of UV-ozone treatment. An adhesion layer of 2 nm of Cr followed by 50 nm of gold was deposited through thermal vapor deposition at 1×10^{-6} Torr with a shadow mask used to define the pattern shown in Fig. S12a. The channel length was set to 2 mm with 200 µm wide gold contacts. Later 100 nm of bismuth was thermally deposited through a different shadow mask at the same pressure. Doped polymers were drop cast on the substrate in the glovebox (see Fig. S12a for area of deposition) and then

transferred to a custom-built vacuum chamber in ambient atmosphere, as shown in Fig S12b, with air exposure typically lasting 2-5 minutes. The pressure in the chamber was held between 1 and 4 Torr for the rest of the measurements. A multi stage Peltier module (TE-2-(127-127)-1.15) is coupled with a TC-48-20 controller and MP-3176 thermistor all purchased from TE Technology, Inc. to control the temperature of the substrates. The Peltier module is thermally connected with the base of the chamber where 4 cooling fluid lines held at -10 °C provide additional cooling and heat removal. Two electrical feedthroughs (Belilove Company–Engineers) are used to bring the electrical wires into the vacuum chamber. Noctua NT-H1 thermal paste was used to ensure good thermal contact between Peltier module, aluminum stage and substrate.

For each Seebeck coefficient measurement the temperature of the stage was held constant for at least 10 minutes before measurement to ensure a constant temperature on the substrate. The temperature gradient was provided by Joule heating of the on-chip heater line while sourcing current between pin 5 and 6 with 4 different applied voltages (2, 4, 8 and 10 V). The potential difference is measured betwen pin 1 and 2 (for polymer) and pin 3 and 4 (for bismuth, which acts as a standard to determine the temperature difference) with two Keithley 2100 6½-digit USB multimeters. By using equation at $\Delta T=\Delta V_{Bi}/\alpha_{Bi}$, the voltage across the bismuth film is converted to a temperature difference. The temperature gradient across bismuth should equal the temperature gradient across the polymer based on the heater line layout and the locations of thermal contact with the underlying Al block. Fig. S12c. shows the thermoelectric voltage of the bismuth film and calculated temperature gradient across the film as a function of time and applied power to heater line at 21°C. At each heater line power increment, the temperature and polymer thermoelectric voltage (following ramp-up) is averaged to obtain a single value as shown in Fig. S12d. These average voltage and temperature measurements at each heater line power increment are plotted and the slope of the linear fit is used to determine the Seebeck coefficient of the polymer film at that substrate temperature.

The temperature response of α for 100 nm films of thermally evaporated bismuth is linear between 100 and 400 K and can be approximately written as $S=-0.123T+S_0$.[58] The temperature difference across our films was calculated based on this equation, with S_0 as -25.3 μV K^{-1}. Additionally, we observed the expected linear dependence of the temperature gradient with respect to the power applied to the on-chip heater line ($P \propto V^2$), as shown in Fig. S12e.[59]

References

39. Zhao, Y., Zhao, X., Zang, Y., Di, C.-a., Diao, Y., Mei, J. Conjugation-Break Spacers in Semiconducting Polymers: Impact on Polymer Processability and Charge Transport Properties. *Macromolecules*, **48,** 2048-2053 (2015).
40. Schroeder, B. C., Kurosawa, T., Fu, T., Chiu, Y. C., Mun, J., Wang, G. J. N*., et al.* Taming charge transport in semiconducting polymers with branched alkyl side chains. *Adv. Funct. Mater.*, **27,** 1701973, (2017).
41. Luo, X., Tran, D. T., Sun, H., Mi, T., Kadlubowski, N. M., Zhao, Y*., et al.* Bis-isoindigos: New Electron-Deficient Building Blocks for Constructing Conjugated Polymers with Extended Electron Delocalization. *Asian J. Org. Chem.*, **7,** 2248-2253 (2018).
42. Boehm, A. M., Wieser, J., Butrouna, K., Graham, K. R. A new photon source for ultraviolet photoelectron spectroscopy of organic and other damage-prone materials. *Org. Electron.*, **41,** 9-16 (2017).

43. Liang, Z., Boland, M. J., Butrouna, K., Strachan, D. R., Graham, K. R. Increased power factors of organic-inorganic nanocomposite thermoelectric materials and the role of energy filtering. *J. Mater. Chem. A*, **5,** 15891-15900 (2017).
44. Podzorov, V., Pudalov, V. M., Gershenson, M. E. Field-effect transistors on rubrene single crystals with parylene gate insulator. *Appl. Phys. Lett.*, **82,** 1739-1741 (2003).
45. Choi, H. H., Rodionov, Y. I., Paterson, A. F., Panidi, J., Saranin, D., Kharlamov, N.*, et al.* Accurate Extraction of Charge Carrier Mobility in 4-Probe Field-Effect Transistors. *Adv. Funct. Mater.*, **28,** 1707105 (2018).
46. Cordischi, D., Occhiuzzi, M., Dragone, R. Quantitative EPR spectroscopy: Comparison between primary standards and application to MgO-MnO and *α*-Al2O3-Cr2O3 solid solutions. *Appl. Magn. Reson.*, **16,** 427-445 (1999).
47. Eaton, G.R., Eaton, S.S., Barr, D.P., Weber, R.T., Quantitative EPR, Springer-Verlag Wien, (2010).
48. Shen, X., Hu, W., Russell, T. P. Measuring the Degree of Crystallinity in Semicrystalline Regioregular Poly(3-hexylthiophene). *Macromolecules*, **49,** 4501-4509 (2016).
49. Frisch, M. J., Trucks, G. W., Schlegel, H. B., Scuseria, G. E., Robb, M. A., Cheeseman, J. R.*, et al.* Gaussian 16 Rev. C.01. Wallingford, CT; (2016).
50. Hariharan, P. C., Pople, J. A. The influence of polarization functions on molecular orbital hydrogenation energies. *Theor. Chim. Acta*, **28,** 213-222 (1973).
51. Perdew, J. P., Burke, K., Ernzerhof, M. Generalized Gradient Approximation Made Simple. *Phys. Rev. Lett.*, **77,** 3865-3868 (1996).
52. Vreven, T., Frisch, M. J., Kudin, K. N., Schlegel, H. B., Morokuma, K. Geometry optimization with QM/MM methods II: Explicit quadratic coupling. *Mol. Phys.*, **104,** 701-714 (2006).
53. Vydrov, O. A., Scuseria, G. E. Assessment of a long-range corrected hybrid functional. *J. Chem. Phys.*, **125,** 234109 (2006).
54. Vydrov, O. A., Scuseria, G. E., Perdew, J. P. Tests of functionals for systems with fractional electron number. *J. Chem. Phys.*, **126,** 154109 (2007).
55. Francl, M. M., Pietro, W. J., Hehre, W. J., Binkley, J. S., Gordon, M. S., DeFrees, D. J.*, et al.* Self‐consistent molecular orbital methods. XXIII. A polarization‐type basis set for second‐row elements. *J. Chem. Phys.*, **77,** 3654-3665 (1982).
56. Stein, T., Kronik, L., Baer, R. Reliable Prediction of Charge Transfer Excitations in Molecular Complexes Using Time-Dependent Density Functional Theory. *J. Am. Chem. Soc.*, **131,** 2818-2820 (2009).
57. Cheema, H., Baumann, A., Loya, E. K., Brogdon, P., McNamara, L. E., Carpenter, C. A.*, et al.* Near-Infrared-Absorbing Indolizine-Porphyrin Push–Pull Dye for Dye-Sensitized Solar Cells. *ACS Appl. Mater. Interfaces*, **11,** 16474-16489 (2019).
58. Mikolajczak, P., Piasek, W., Subotowicz, M. Thermoelectric power in bismuth thin films. *phys. status solidi (a)*, **25,** 619-628 (1974).
59. Yoshida, M., Iizuka, T., Saito, Y., Onga, M., Suzuki, R., Zhang, Y.*, et al.* Gate-Optimized Thermoelectric Power Factor in Ultrathin WSe2 Single Crystals. *Nano Lett.*, **16,** 2061-2065 (2016).

Acknowledgements

K.R.G., Z. L., T.L., A.M.B., and A.A. acknowledge the donors of The American Chemical Society Petroleum Research Fund for partial support of this research (Grant # 57619-DNI10). K.R.G., A.A., K.N.B. and C.R. acknowledge support from the National Science Foundation (DMR-1905734). U.S.R and C.R. acknowledge partial support from the Office of Naval Research Young Investigator Program (N00014-18-1-2448). J.L.H. and A.A. were supported through DOE 0000223282 for performance of the low-temperature electrical conductivity measurements. Supercomputing resources on the Lipscomb High Performance Computing Cluster were provided by the University of Kentucky Information Technology Department and the Center for Computational Sciences (CCS). V.P. and H.H.C. acknowledge support from the National Science Foundation under the grant ECCS-1806363. H.H.C. acknowledges partial support from the Center for Advanced Soft-Electronics at Pohang University funded by the Republic of Korea's Ministry of Science, ICT and Future Planning as Global Frontier Project (CASE-2011-0031628). J.M. and X.L. appreciate the support from the NSF (NSF CAREER award number 1653909).

Author contributions

K.R.G. and Z.L. proposed the ideas, designed the experiments, and prepared the manuscript. K.R.G supervised the project. Z.L. carried out the Seebeck coefficient and electrical conductivity measurements and prepared samples for UV-vis-NIR, UPS, IPES, and Hall effect measurements. Z.L., T.L., and A.M.B. performed the UPS and IPES measurements. H.H.C. and V.P. carried out Hall effect experiments and helped in

interpreting the Hall effect data. X.L. and J.M. synthesized DPP-containing polymers. X.L. and T.L. measured the UV-vis-NIR absorbance spectra. U.S.R. and C.R. performed the DFT calculations. Z.L., J.A.H., T.L., and K.N.B. prepared samples for EPR or measured EPR spectra. D.S., J.L.H., A. Ansary and Z.L. performed the temperature dependent electrical conductivity measurement. A. Abtahi measured temperature dependent Seebeck coefficients and prepared and characterized $FeCl_3$ doped Spiro-OMeTAD samples. All authors analyzed data and helped with the writing of the manuscript.

Data availability

Source data for Fig. 2 - 5 are provided with the paper. Additional data are available from the corresponding author upon reasonable request.

Competing interests

The authors declare no competing interests.

Additional information

Supplementary information is available for this paper.